Università degli Studi di Padova

Dipartimento di Fisica e Astronomia "Galileo Galilei"

Master's Degree in Astrophysics and Cosmology

The relationship between binaries and blue stragglers: a photometric analysis of NGC 6101

Supervisor:
Prof. Antonino P. Milone

Candidate:
Isabella Maria Grimaldi
Student ID: 2071453

Academic year 2023/2024

"The universe will give you more of what you pay attention to."

— Rivers Cuomo

Abstract

Several studies have laid groundwork for the fact that the populations of binary systems and blue straggler stars (BSSs) are related, particularly in globular clusters (GCs). Formation channels proposed for BSSs, stars which appear to be more massive and hotter than the rest of the population, can be traced at least partially back to the evolution of binary systems. Furthermore, Milone et al. 2012 found that both BSSs and binaries anti-correlate with the mass of their host cluster, in addition to a correlation between the binary fraction and BSSs frequency in cluster cores. This connection, although apparent, has yet to be directly quantified. In this thesis, I utilized HST observations, in the filters F814W and F275W, to derive high precision photometry and astrometry of the globular cluster NGC 6101, in order to construct mass functions (MFs) as a new approach to remedy this situation. In relating these MFs with each other, a measurable connection between the binary population and BSSs can be determined. Three methods to calculate this were employed, involving estimates for the overall average number of binaries and BSSs, as well as through extrapolating the binary MF out to the range of the BSS MF and doing a bin by bin comparison. All methods found that roughly 10% of binaries may have evolved into BSSs over time. As such, this has provided a meaningful inquiry into the BSS-binary connection for NGC 6101. Expanding this approach for a larger dataset of GCs, as well as comparison to statistical simulations, could then be used to examine how the BSS-binary populations change with respect to GC parameters.

Contents

List of figures

List of tables

List of abbreviations

ACS ..... Advanced Camera for Surveys
AGB ..... Asymptotic Giant Branch
BSS ..... Blue Straggler Star
CMD ..... Color-Magnitude Diagram
CTE ..... Charge Transfer Efficiency
DR3 ..... Data Release 3
ESA ..... European Space Agency
FoV ..... Field of View
GC ..... Globular Cluster
HB ..... Horizontal Branch
HST ..... Hubble Space Telescope
JWST ..... James Webb Space Telescope
LF ..... Luminosity Function
MF ..... Mass Function
MS ..... Main Sequence
MSTO ..... Main Sequence Turn-Off
NASA ..... National Aeronautics and Space Administration
PSF ..... Point-Spread Function
RGB ..... Red Giant Branch
SGB ..... Sub-Giant Branch
WD ..... White Dwarf
WFC/WFC3 ..... Wide-Field Camera/Wide-Field Camera 3
UVIS ..... Ultra-Violet Visible

1 Introduction

1.1 Globular clusters

Globular clusters (GCs) are large, dense collections of stars gravitationally bound together, typically very old and bright ($M_v \sim -7$) (Gratton et al. 2019 [1]). Historically, they were considered the best example of simple stellar populations (SSPs): groups of stars that share the same age, initial chemical composition, and initial mass function (Renzini & Buzzoni 1986 [2]). Although in current times it has been found that GCs usually host multiple populations (Greggio & Renzini 2011 [3]), they remain an excellent source for in-depth analysis of different stellar objects. Often found in the galactic halo, they are the oldest objects in the local Universe for which accurate ages have been determined, with formation times corresponding from $z \sim 5$ to into the reionization era (see Renzini 2017, and references therein [4]). As such, it is likely that they played a pivotal role in the formation of the Milky Way; careful investigation into GCs can tell us not only about stellar evolution, but galaxy formation as well.

1.2 Binary systems in GCs

The stellar population of any cluster cannot be sufficiently described without the acknowledgment of binary systems. It is known that close to 50% of all stars are members of a binary (or multiple) star system (Renzini & Buzzoni 1986 [2]), which can have profound effects on their evolution and the presence of different exotic stellar objects. In globular clusters especially, the environment is so dense that many stars in binary systems are so close together that their individual magnitudes cannot be resolved, instead resembling a single point source. As stated in Milone et al. 2012 [5], this magnitude, m_{bin}, can be

described as

$$m_{bin} = m_1 - 2.5 \log \left(1 + \frac{F_2}{F_1}\right) \tag{1.1}$$

where m_1, m_2, F_1, and F_2 are the magnitude and flux of each star:

$$\begin{aligned} m_1 &= -2.5 \log F_1 \\ m_2 &= -2.5 \log F_2 \end{aligned} \tag{1.2}$$

This observed magnitude is of course brighter than the magnitude of a single unresolved star. For equal-mass binaries in a SSP, $m_1 = m_2$ & $F_1 = F_2$, and Equation 1.1 reduces to

$$\begin{aligned} m_{bin} &= m_1 - 2.5 \log \left(1 + \frac{F_2}{F_1}\right) = m_1 - 2.5 \log (1+1) \\ m_{bin} &= m_1 - 0.752 \end{aligned} \tag{1.3}$$

Therefore a binary system can appear up to 0.752 magnitudes brighter. Considering that in SSPs, the flux is directly related to the stellar mass, we can then define a mass ratio, $q = \frac{M_2}{M_1}$, where M_1 & M_2 are the mass of each respective star. For systems with $q \geq 0.5$, this has a noticeable effect on the color-magnitude diagram (CMD): binaries composed of main-sequence (MS) stars will appear to the top of the MS, as illustrated in Figure 1.1.

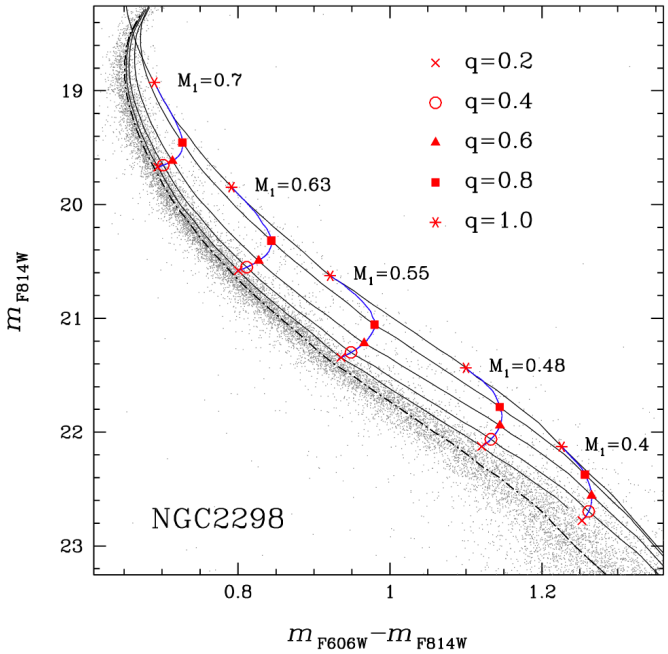

Figure 1.1: Binaries along the main-sequence. A model of the positions for unresolved main-sequence binaries, in relation to their mass ratio q, for the globular cluster NGC 2298. The larger q is, the higher up the unresolved binaries will appear. Image from Milone et al. 2012 [5].

The significance of binaries in GCs cannot be overstated: Milone et al. 2012 & 2016 [5, 6] demonstrated that they have been found to correlate with the cluster mass — GCs with a lower luminosity (and therefore smaller visible mass) have higher binary fractions. However, observations have shown that the binary fraction in a given GC tends to be smaller than in other environments. The dense, high velocity environment of GCs makes close encounters more prevalent than in the field and likely contributes to the disruption of binary systems (Heggie & Hut 2003 [7]). These studies [5, 6] also suggested that the binary fraction does not correlate with the age of the cluster, but this is in contradiction to some others, which found that the binary fraction is higher for younger GCs (Sollima et al. 2007 [8]; Ji & Bregman 2015 [9]). The evolution of binary systems is thought to contribute to the presence of various exotic stellar objects found in GCs, such as millisecond pulsars, X-ray binaries, cataclysmic variables, and blue straggler stars (Gratton et al. 2019 [1]). Blue stragglers specifically have also been found to anti-correlate with the luminosity of their host GC, suggesting a deeper relationship between them and the binary population (Piotto et al. 2004 [10]; Milone et al. 2012 [5]).

1.3 That's BSS

One peculiarity frequently spotted in GCs are blue straggler stars (BSS). First observed by Allan Sandage in the galactic cluster M3 (Sandage 1953 [11]), these are stars that appear to be bluer and brighter (and therefore more massive) than the rest of the cluster, spotted on the top and to the left of the main sequence turn-off (MSTO)(see Figure 1.2). Usually they appear right near the MSTO to ~ 2 magnitudes brighter, but they have been observed up to 3 magnitudes brighter (Sills 2016 [12]). BSSs are a common phenomena, appearing all across the local Universe: in the galactic field, open and globular clusters, even dwarf galaxies in the Local Group. Evidently, whichever mechanism(s) responsible for producing them are efficient, notwithstanding the environment (Cassisi & Salaris 2013 [13]). In GCs, they often follow a specific distribution pattern, on average more concentrated than the rest of the stellar population — the number of blue stragglers peaks at the center, decreasing until a minimum radius, r_{min}, then increases slightly to a constant value towards the edge of the cluster (Sills 2016 [12]). In CMDs constructed from UV bands, the brightness is dominated by BSSs (Ferraro et al. 2001 [14]). Ferraro et al. (2012) [15] ascertained that this can allow blue stragglers to act as "test probes" to explore the dynamical evolution of GCs. Due to their high density, GCs are subject to dynamical friction, where stars lose energy over time from gravitational collisions, leading more massive objects to move towards the center (Binney & Scott 2008 [16]). They found the location of r_{min} to increase as the cluster became more dynamically evolved. One starts with a flat distribution (no r_{min} present) for "dynamically young" clusters, until r_{min} is at the cluster boundary for "dynamically old" clusters (Sills 2016 [12]).

1.3.1 Formation channels

The intriguing nature of BSSs lies in their unique position on the CMD. As part of the same population as the rest of the cluster, they are more massive than can be explained following the standard process for

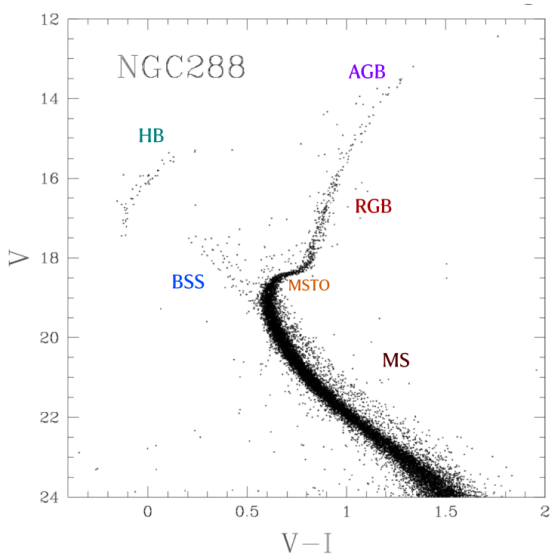

Figure 1.2: Blue stragglers on the CMD. A CMD constructed for the globular cluster NGC 288. The Main Sequence (MS), Main Sequence Turn-off point (MSTO), Red Giant Branch (RGB), Asymptotic Giant Branch (AGB), Horizontal Branch (HB) can be clearly seen. One can also see the Blue Straggler Stars (BSSs) to the left and the top of the MSTO, "straggling" behind the rest of the main sequence. Assuming they are the same age as the rest of the cluster, BSSs must be more massive than their peers in order to explain their position. CMD taken from the Stellar Astrophysics lecture notes of Antonino P. Milone, 2023.

stellar evolution. Therefore, their origins must be carefully investigated. It is theorized that there are two main formation channels:

1. *Mass transfer/Coalescence of binary systems.*
   In this channel, blue stragglers are formed through the evolution of wide or isolated binary systems. This can occur when one of the stars in a binary has evolved off the main-sequence into a red giant, expanding into its Roche lobe. Once the radius has increased so much that material has overflowed the Roche lobe, it is no longer gravitationally bound to the star and will begin to transfer material to its stellar companion through the Lagrangian point. This is a gradual process, where the new blue straggler is a main-sequence star with an enhanced H-envelope, allowing it to burn for longer than other MS stars. BSSs deriving from this process are referred to as primordial BSSs, in the sense that they are not a consequence of dynamical evolution of the binary system (Salaris & Cassisi 2013 [13]). The surface material of these primordial blue stragglers is thought to stem from deep inside the donor star, where the CNO process occurs. This would leave them depleted in carbon and oxygen, but enhanced in nitrogen (Ferraro et al. 2015, and references therein [17]) which has indeed been observed (see Ferraro et al. 2006 [18]). Close binaries can also create BSSs, in which the system merges over time due to loss in angular momentum from stellar winds. In this case, the resulting blue straggler will present similarly to BSSs produced from stellar collisions (Davies 2016 [19]).

2. *Stellar Collisions/Mergers.*
   The second channel of BSSs is formed through runaway stellar collisions. To create a blue straggler, these collisions must occur at rates high enough for a steady production of mergers with little mass loss. This can arise in the high-density environment in GC centers, where up to 10% of stars will have been involved in a collision during their lifetime (Davies 2016 [19]). Within this channel there are two pathways to development: mass transfer from a direct collision of two stars, and mass transfer from a stellar encounter with a binary system. As a product of dynamical evolution, the resulting stars are often referred to as collisional or dynamical BSSs (Salaris & Cassisi 2013 [13]). Dynamical blue stragglers are theorized to have limited mixing of the stellar cores/envelopes, and therefore maintain a similar chemical composition as their progenitors (Lombardi et al. 1996 [20]).

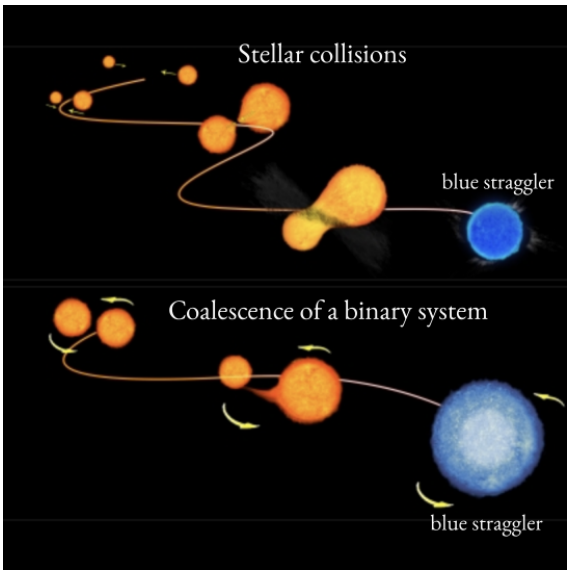

Figure 1.3: Blue straggler formation channels. A depiction of the two different formation channels for BSSs: stellar collisions (top), and coalescence of binary systems (bottom). Image taken from ESA[1].

Both of these formation channels are expected to be responsible for the production of BSSs, depending on the environment in which they develop. Furthermore, some studies (e.g. Mapelli et al. 2006 [21]) theorized these mechanisms could act simultaneously within the same GC. Observations from Ferraro et al. 2009 [22] concur with this, as they detected two parallel sequences of BSSs in the globular cluster M30 — a bluer population resulting from stellar collisions, and a redder population from ongoing coalescence events. A question now arises — which formation process(es) dominate? Many studies suggest binary evolution is the preferred mechanism. Piotto et al. 2004 [10] found that the frequency of blue stragglers is not related to the rate of stellar collisions in GCs, implying the collisional channel is not the primary formation channel. Knigge et al. 2009 [23] discovered a correlation between the number of blue stragglers within the cluster core and the total core mass, surmising that binary evolution

[1] `https://sci.esa.int/web/hubble/-/46222-the-formation-of-blue-stragglers`

must be the primary mechanism for BSSs. Stellar collisions are likely only a notable formation path for the most massive clusters, or those brighter than $M_v \sim -9$, where the environment is rife with stellar interactions that disrupt binary systems at greater rates, making them less responsible for the BSS population (Ferraro et al. 2015 [17]). However, not all the data provides such clear results; although Leigh et al. 2013 [24] agreed there is a strong correlation between the number of BSSs and the mass of the cluster core, they were unable to find a stronger direct correlation between the number of BSSs and the binary fraction.

1.4 The BSS - Binary connection

As mentioned in the previous sections, the stories of BSSs and binaries are certainly intertwined.

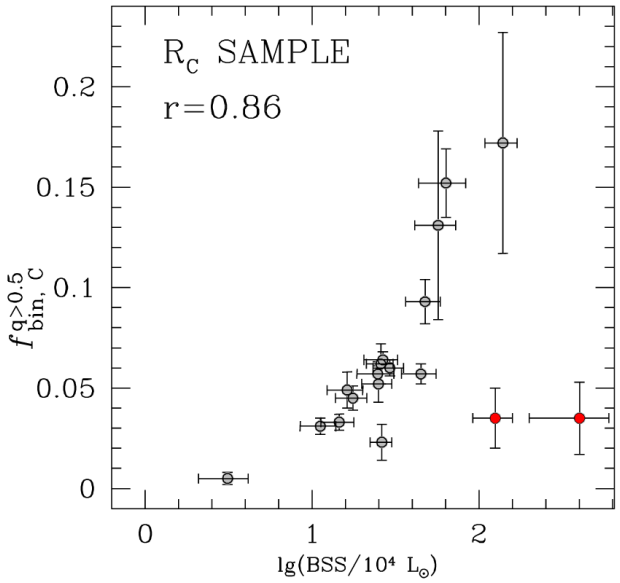

Figure 1.4: The BSS-Binary Connection. A plot of the binary fraction as a function of the concentration of BSSs located in the core for several GCs, from Milone et al. 2012 [5]. There is clearly a positive correlation between the number of binaries and blue stragglers found.

Milone et al. 2012 [5] found that not only do they both anti-correlate with the mass of the host cluster, but that the binary fraction and BSS frequency are also directly correlated in cluster cores (see Figure 1.4). As Section 1.3.1 discusses, the formation theories for blue stragglers are often reliant on binaries — BSSs formed from both coalescence and stellar collisions can hail from interactions or evolutions of binary systems. Binary evolution, dynamical or otherwise, must be connected to the production of BSSs. Literature suggests BSSs from binaries could be the dominant production process in GCs, albeit with some uncertainties. Obviously, this BSS-binary connection must be investigated further, to shed

light not only on how blue stragglers are formed, but on the greater evolutionary mechanisms governing binaries and globular clusters themselves.

1.4.1 Thesis layout

This thesis proposes a new approach to try and quantify the relationship between the BSS and binary population. To address this, I constructed initial mass functions for both populations, as a rough determination of how many binary systems may have evolved into blue stragglers over time. The following chapters will describe this process, and is organized as follows: after providing a background to the project in chapter 1, chapter 2 both discusses the dataset and illustrates the data reduction process, after which chapter 3 describes the data analysis that was conducted. Finally, chapter 4 discuses the results of the project and how they fit into the greater scientific exchange.

2

Data & Data Reduction

2.1 NGC 6101

The globular cluster NGC 6101 was chosen as the target for this project. NGC 6101, sometimes referred to as Caldwell 107, is located in the halo of the Milky Way, was first discovered in the 19th century by James Dunlop (Cozens et al. 2010 [25]). The cluster is metal-poor, with an iron abundance [Fe/H] $= -1.98$ (Carretta et al. 2009 [26]). A study (Cohen et al. 2011 [27]) of the the variable RR Lyrae stars within the cluster determined it to be an Oosterhoff type II cluster — a cluster classification marked by an RR Lyrae pulsation period of $\sim$ 65 days and low metallicity (Salaris & Cassisi 2013 [13]). However, NGC 6101 has also been found to have retrograde motion (Rutledge et al. 1997 [28]), which is unusual for Oosterhoff type IIs and for metal-poor galactic GCs in general. As such, the authors of [27] stipulate the cluster may have originated from interactions between the Milky Way and Canis major.

Through a calculation of the radial distribution of BSSs, MS binaries, and the MF, Dalessandro et al. 2015 [29] found no evidence for any mass segregation, suggesting NGC 6101 is a dynamically young cluster. Interestingly, N-body simulations suggest this may be due to a high population of stellar-mass black holes (Peuten et al. 2016 [30]). Following the theory put forth by Ferraro et al. 2012 ([15]) (see Section 1.3), its young dynamic age indicates a flat distribution of both the binary and blue straggler population. Additionally, NGC 6101 has a sizable amount of both binary and blue straggler stars (Dalessandro et al. 2015 [29]). These both make the cluster an excellent candidate to test the approach used in this thesis. Furthermore, for the purposes of this study NGC 6101 can be approximated with an SSP, as any multiple populations within such a low-metallicity cluster would be difficult to discern (Gratton et al. 2019 [1]). An analysis of this cluster would consequently provide a clear, relatively simple environment to test this approach to analyze the relationship between blue straggler and binary populations.

2.2 The Instrument

Like the thousands of studies which came before it, this project would not be possible without the Hubble Space Telescope (HST). HST[1] is a joint NASA/ESA space-based observatory, which has been in service since 1990. It observes in the ultraviolet, optical, and infrared, at ~115 – 2500 nm. It was the most advanced space-based observatory until JWST. Two of its instruments are relevant for this thesis:

- *Advanced Camera for Surveys (ACS)/ Wide Field Camera (WFC)*
  ACS has been on HST since 2002. It has two channels still in operation; relevant to this work is the WFC channel, which observes in the optical to infrared at 350 – 1100 nm. It has an average pixel size of 0.04″, giving a FoV of 202 x 202″[2]. ACS was chosen for its sensitivity at redder wavelengths (ACS Data Handbook [31]).
- *Wide Field Camera 3 (WFC3)/ Ultra-Violet Visible (UVIS)*
  WFC3 has been on HST since 2009. It has two channels; relevant to this work is the UVIS channel, which observes in the ultraviolet to optical at 200 – 1000 nm. It has an average pixel size of 0.05″, giving a FoV of 162 x 162″[2] (WFC3 Data Handbook [32]). UVIS was chosen to highlight the population of BSSs, which have been shown to peak in the UV (see Section 1.3).

2.3 The Data

This project utilized archival HST data products[2] from two separate proposals and two different cameras to obtain observations in both the filter F814W, taken in the infrared, and the filter F275W, taken in the UV. Originally obtained as part of HST Proposal 13297, the dataset in F275W was taken on WFC3/UVIS. Similarly, the dataset in F814W, taken on ACS/WFC, was originally obtained as part of HST Proposal 10775. Both datasets are observations of the center of NGC 6101, at angular separations of $\sim 0.1''$ (Figure 2.1). Specifically, I took use of the `_flt.fits` files, which had already been flat-fielded and corrected for Charge Transfer Efficiency (CTE), for the data analysis and reduction. I additionally retrieved the `_drc.fits` files, also flat-fielded and corrected for CTE as well as geometric distortion, to aid in the calibration of the data from instrumental to astronomical magnitude (see Section 2.7). The details of the files downloaded can be seen in Table 2.1.

2.4 PSF Photometry

The data was reduced using a series of `Fortran` programs, following the procedure developed by Anderson et al. (see Anderson & King 2000 [33]; Anderson & King 2006 [34]; Anderson et al. 2008 [35]). The first step was using `flt2wj2` to convert the `_flc` files to `_wjc` files. This converts a multi-layered

[1] `https://science.nasa.gov/mission/hubble/overview/about-hubble`
[2] All files were downloaded from the MAST website: `https://mast.stsci.edu`

(a) F275W

Filename	Date	Time	Exp.
icau34goq	04/04/14	09:59:59	851
icau34grq	04/04/14	10:16:24	851
icau35dmq	25/05/14	01:52:09	851
icau35dpq	25/05/14	02:08:34	851
icau36kmq	29/06/14	14:37:03	889
icau36kpq	29/06/14	14:54:06	889
icau37poq	14/08/13	08:54:03	940
icau37p3q	14/08/13	09:11:57	940
icau38vuq	28/02/14	16:11:39	889
icau38vxq	28/02/14	17:28:03	889

(b) F814W

Filename	Date	Time	Exp.
j9l917iwq	31/05/06	16:32:03	35
j9l917ixq	31/05/06	16:34:56	380
j9l917izq	31/05/06	16:43:59	380
j9l917j1q	31/05/06	16:53:02	380
j9l917j3q	31/05/06	17:52:48	380
j9l917j5q	31/05/06	18:01:51	380

Table 2.1: The Data. Selected keywords from the header of the `_flc.fits` files, displaying: the filename, date and time of observation, and exposure time (in seconds). There were 10 files from F275W, and 6 files from F814W.

`.fits` file into a single 4096 x 4096 image, which will allow the data to be reduced more efficiently and was required for the programs used (Sohn et al. 2012 [36]).

The procedure relies on Point-Spread Function (PSF) photometry to obtain measurements of the flux and positions of all the sources in an image. PSFs are a representation of the spread of light the instrument produces for each point source. The first step is `img2psf`, which constructs effective Point Spread Functions (ePSFs) — continuous two-dimensional functions that tell us what fraction of a star's light will fall within a pixel that is offset by the star's center at $(\Delta x, \Delta y)$ (Anderson et al. 2008 [35]). Deriving the ePSF is a multi-step, iterative process, alternating between constructing positions and flux of each source to construct an ePSF, using it to more accurately measure the parameters, which are then used to re-derive the ePSF. More specifically, it divides the image into a grid with a number of cells, and using a "library PSF" as a first guess, fits the isolated, bright, and unsaturated stars within the grid to the PSF model (Milone et al. 2023 [37]). Next, through a linear least-squares fitting of the residuals, it remeasures the positions and flux for each source and averages together the values it found to improve the PSF model (Anderson & King 2000 [33]). The program takes several arguments:

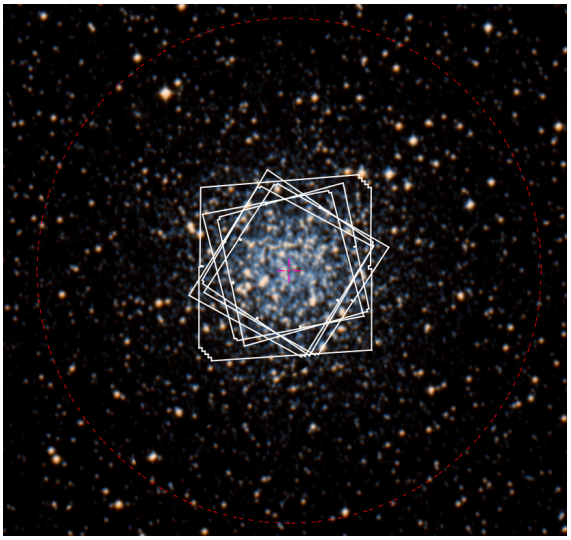

Figure 2.1: Visualizing the data. Footprint of the datasets used, overlayed over their position in NGC 6101. They were all observations of the center of the cluster.

1. **`HMIN`** — Determines the minimum distance (in pixels) between sources to be considered. It was set to 12 to ensure it used isolated stars.
2. **`FMIN`** — Determines the minimum amount of of flux (in counts) needed to consider a source. To ensure bright sources were used, it was set to 5000 for long exposures. For short exposures[3] it was set to 3000.
3. **`PMAX`** — Determines the maximum amount of flux (in counts) to consider a source. It was set to 54000 in order to exclude saturated stars.
4. **`QMAX`** — Determines the maximum "badness" value allowed for Q, a quality of fit parameter. For the first run, it was set to 0.3.
5. **`NSIDES`** — Determines the number of cells (N x N) in the grid it will divide the image into. It was set to 2.
6. **`PSFFILE`** — Here, one would add a PSF file as a starting point for the program to improve upon. For this I used the "library PSFs" provided by Anderson & King 2006 [34] for each filter.

It then returns a PSF file. A correctly generated PSF should show approximately circular sources, with little to no distortion or spread (see Figure 2.2).

2.4.1 QFIT

Now equipped with a PSF, I then used the program `img2xym` to generate a `.xym` file containing the positions and instrumental magnitudes for every point source in an image. The program takes similar

[3] There was only one file, in F814W, which had a short exposure time. See Table 2.1 for more details.

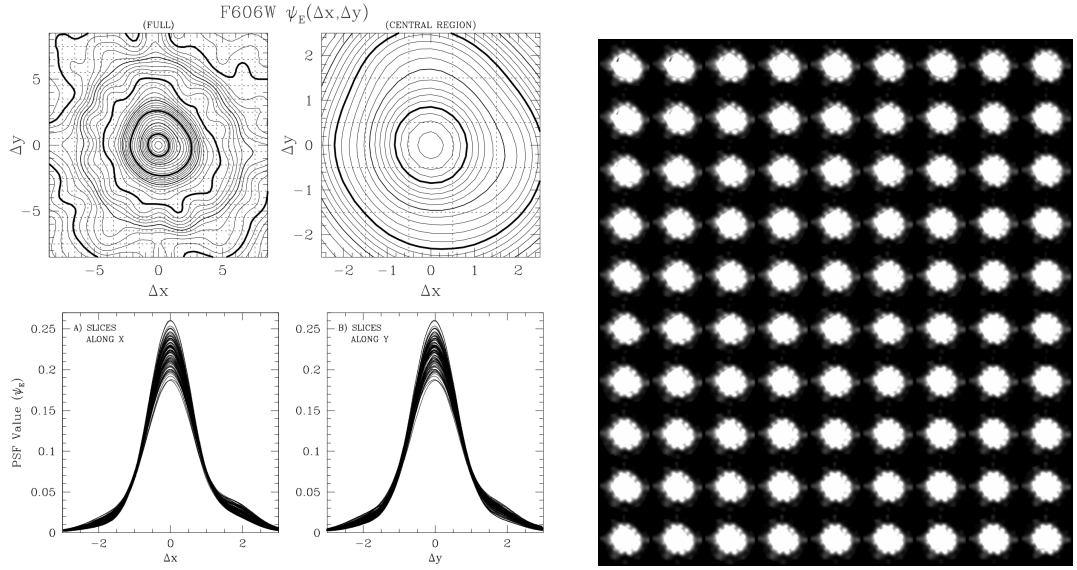

Figure 2.2: Visualizing a PSF. On the left, a contour plot and *x* and *y* profiles of a PSF, taken from Anderson & King 2006 [34]. On the right, the PSF file that was generated from file `j91917iwq`, in F814W.

arguments as `img2psf`, but as we now want a measurement of every point source in the image, the inputs are more relaxed:

1. **`HMIN`** — Now set to 5, to include sources close together.
2. **`FMIN`** — Now set to 50, to include faint sources.
3. **`PMAX`** — Now set to 10^9, to include saturated stars.
4. **`PSFFILE`** — Here, it takes the PSF file that was just generated with `img2psf`.

In addition to the positions and magnitudes, the `.xym` file will also contain the value of Q for each point. As mentioned previously, Q is related to the quality of the fit for the PSF generation. The larger the value of Q, the more likely the source is not a star, but some other source the detector picked up, such as artifacts, cosmic rays, or spikes in noise (Anderson & King 2006 [34]). It is then beneficial to create Qfit plots as seen in Figure 2.3, which plot the instrumental magnitude vs. Q for each point. Visually, the true stellar sources will make somewhat of an exponential curve upward, where the bad sources will appear as a "cloud" to the top and bottom of this curve. I then used the Qfit plots for two steps. First, I plotted my `QMAX` value on top, to confirm whether the initial input was sufficient — if it was too large, I included too much of the "bad" sources to generate the PSF, and if it was too small, I excluded some of the real stellar sources in the PSF generation. If it was necessary to change `QMAX`, I then reran `img2psf` and `img2xym` before continuing. For the files in F814W, I had to rerun with a `QMAX` of 0.4. However, for F275W I found that the initial guess of 0.3 was sufficient. Second, I used these plots to manually select the points corresponding to the true sources and generate new `.xym` files only containing these points.

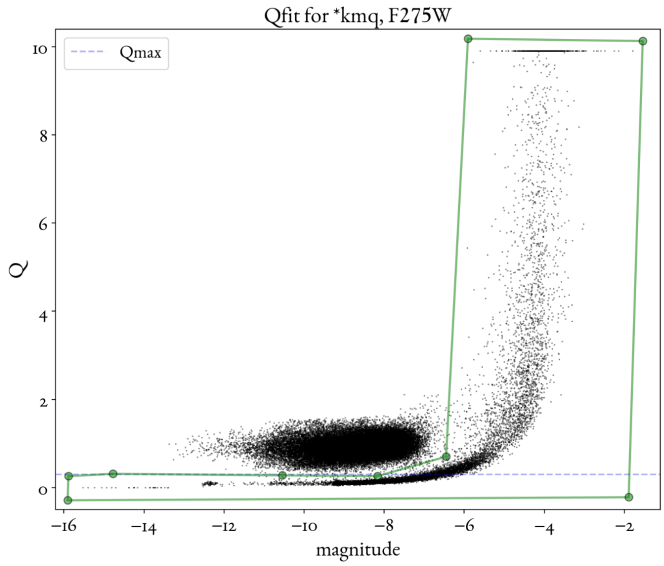

Figure 2.3: Qfit plot. The Qfit plot generated for file `icau36kmq`, in F275W, with instrumental magnitude on the x-axis and the Q value on the y-axis. Real stellar sources appear to form an exponential-like curve, while points that can be attributed to noise, artifacts, or cosmic rays appear as a cloud of points on top. The real stellar sources were manually selected[4], as seen by the green box. `QMAX`, the maximum amount of "badness" allowed when constructing the PSF, is also overlayed; for F275W the value 0.3 was sufficient to remove false sources while still including real sources.

2.5 Image Stacking & Alignment

Having now extracted all of the necessary data points into `.xym` files, three subsequent programs were used to stack and align the images to generate a single dataset. Similar to the previous steps, these programs are an inherently iterative process — they must be run numerous times to improve upon their result and ensure that the next step of the process runs as efficiently and accurately as possible.

The first program, `xym2mat`, aligns all images from one filter together. The procedure searches for matches in position and flux between images, using 6 point linear transformations to move an image into the reference frame. It then searches for similar triangles between a star found in an image and the reference frame to find common stars between them. It takes two arguments. The first one is a file, `IN.xym2mat`, which lists all the `.xym` files it will align, as well as which filter and camera the images came from. The first image on the list is used as a reference frame to which the other files will be aligned to. Additionally, the last column in this file lists the magnitude range of sources that will be included in the process. For the first run of the program, I included all bright sources, including saturated stars, to create a "first guess" of the transformation: the magnitude range was set between −99 and −9 for F275W, and −99 and −11 for F814W. The second argument is a number which represents the amount

[4]The sources were selected with `PolygonSelector`: `https://matplotlib.org/stable/gallery/widgets/polygon_selector_demo.html`

of pixel error allowed between the reference image and the image when aligning. As a first guess, this was set to 15 — this means that for a given source, there was a maximum difference of 0.45 pixels allowed between its position in the reference frame and an image. The program then returns `MAT.00*` files, one for each image which was aligned. As well as positions, these files contained the residuals (i.e. the pixel difference) in x and y. Before running the program again, the x and y residuals from these files were plotted to see how the pixel dispersion looked for each image. As seen in Figure 2.4, this dispersion should appear as a blob, and a circle with radius corresponding to the maximum pixel error should be able to encapsulate all of the points. If not, or if the blob is much more concentrated than the circle, the maximum pixel error is adjusted accordingly for the next run. Additionally, saturated stars are removed (changing the range to end at −13.5 instead of −99) for the second run, and the program improves upon the initial transformation to obtain measurements for all stars.

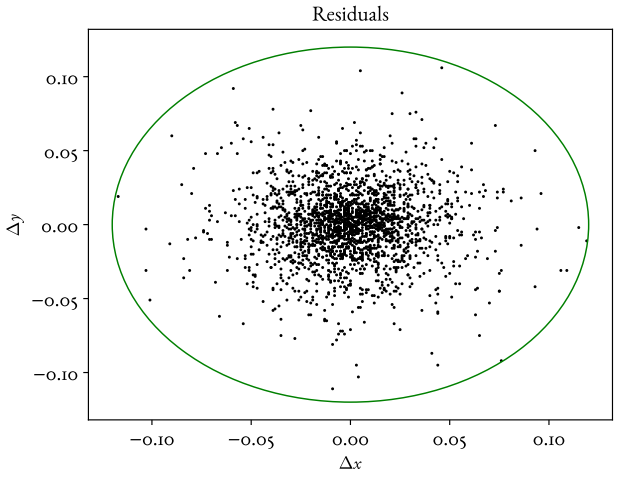

Figure 2.4: Residuals. The plot of residuals between the image `icau36kpq` and the reference frame, image `icau34goq`, in F275W. As it can be seen with the circle overlayed, the dispersion was found to be a bit more concentrated for these images, so for the second run the maximum error allowed was 0.12 instead of the original 0.15. For F814W, the pixel error instead had to be increased slightly to 0.20 to make sure all points were included.

The next program, `xym2bar`, stacks the newly aligned images in one filter together, generating one dataset of the fluxes and positions for all points. It also takes two arguments, the first of which is a similarly structured `IN.xym2bar` file. It lists all of the images to be stacked, but without a reference frame included. Following the same process, the magnitude constraints are relaxed for the first run, allowing saturated stars. The second argument tells the program the minimum number of files a source needs to appear in to be included. For F275W, which had 10 files, it was set to 3. Since there was one short exposure file in F814W, it was set to 1, to make sure that file is still incorporated in the final dataset. The program then returns a `MATCHUP` file, which contains one set of positions, instrumental magnitudes, and residuals for the dataset. The positions, magnitudes, and residuals for each are then plotted to check the program ran correctly — the positions plotted will show the FoV for all the images on top of each

other, and the residuals in position should be close to 0 for well-measured stars (see Figure 2.5). After verifying, the program is rerun without saturated stars to strengthen the transformation. To deal with the mix of long and short exposures in F814W, the magnitude range for the short exposure file is first corrected for the offset in magnitude (about 2.5), and saturated stars are still included in the second run, to ensure no sources are missed.

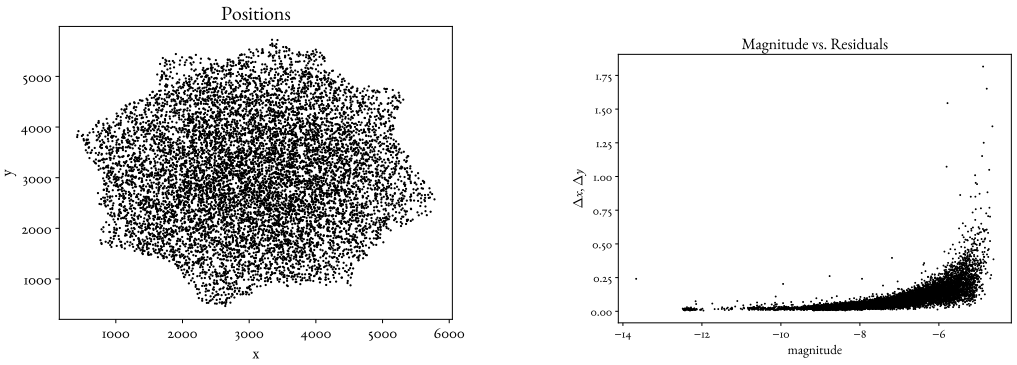

Figure 2.5: `MATCHUP` Plots. Some of the plots generated using the `MATCHUP` files to check if `xym2bar` ran correctly, from F275W. On the left, a plot of the x and y positions of the file. The layout of the points clearly matches the different images, as the FoV changed slightly as the camera moved. On the right, the instrumental magnitude plotted against the residuals in x and y. The residuals are close to 0, only increasing for dimmer, less well-measured stars.

Now that the images within each filter have been stacked and aligned, the program `xym1mat` is used to obtain all stars that appear in both filters, convolving the datasets together. This program takes several arguments, the first of which is the `MATCHUP` file for the "master" catalog to which the other file will be checked against — usually this is the filter with the most amount of stars. Since more stars will always be observed in the infrared, the master catalog was chosen to be F814W. The second argument is simply the `MATCHUP` file from the other filter, and the third argument limits the values for the magnitudes to be used. In the first run, the magnitude range will include only the brightest stars (-99 to -11 for F814W, and -99 to -7 for F275W) for the initial match-up of the filters. The program also takes an argument to set the maximum amount of pixel difference allowed between two frames for an image, which was set to 5, as well as one for the maximum number of iterations, which was set to 21, a number high enough to guarantee the program converges properly. For the second run, the arguments hold, except now all magnitudes are included to obtain a complete calculation. The program then returns a series of files, the most pertinent of which is the `.lnk` or "linker" file, which contains the coordinates and fluxes of every star which appear in both filters.

2.6 Change of Coordinates

In order to evaluate and compare the data in a scientific context, it is crucial to convert the instrumental positions and magnitudes into a proper astronomical system. The first step was to convert the arbitrary

coordinates from the detector into the Gaia reference frame. Gaia, a space-based observatory led by ESA, has been measuring the positions of celestial objects since 2014, creating the most comprehensive database of proper motions to date. This makes it an invaluable tool for coordinate transformations (Gaia Collaboration 2016, 2023 [38, 39]). I started with downloading the positions and magnitudes of all the sources Gaia detected in the area of NGC 6101 from Gaia Data Release 3[5]. Then, utilizing the programs from Section 2.5, I transformed the coordinates following these steps:

1. First, I used a file containing the Gaia proper motions as the master frame, and the `MATCHUP` file for F814W as the other frame. I first ran it for only bright sources, and then again for all sources, following the same routine as before. It then returns a linker file with Gaia positions, but F814W magnitudes.
2. Using this new linker file, I plotted the residuals of the positions (see Figure 2.6). These values cluster around zero, forming a blob, and any points far away from this blob — that is, stars whose proper motions vary greatly from the average — are field stars. I removed any points fitting this condition to ensure I only had positions for the cluster at hand. Additionally, I shifted the coordinates by a constant so all of my positions would be positive values. After these corrections, I am left with a new "Master" file to continue with.
3. Next, I reran the `xym2mat` & `xym2bar` procedures for the images in F814W, but now with the Master file from the last step as the reference frame, including saturated stars in the magnitude range. I then repeated this process, but removed saturated stars from the program arguments. This process returned a final `MATCHUP` file for F814W.
4. I repeated the process in Step 3, but for the images in F275W. The new reference frame used is now the F814W `MATCHUP` file generated in the last step.
5. I now had the `MATCHUP` files for both filters, containing the stellar positions in the Gaia reference frame. I then used these files to rerun the process for `xym1mat` once more, returning a final linker file containing the entire dataset in the proper coordinates.

2.7 Magnitude Calibration

The last step of the data reduction was to calibrate the magnitude of the sources. Up to this point, the stellar magnitude has been expressed by instrumental magnitude, which stems from the number of counts observed by the detector. This value, however, is unphysical; it will vary from detector to detector. To instead express the magnitude in a standard photometric system, it necessary to calculate zero-points: the amount of magnitude that will produce one count per second for a given source (HST Data Handbook [40]). To calibrate the magnitude to the Vega system, which expresses magnitude in an absolute reference frame (with respect to the magnitude of the star Vega), I used the following equation,

$$M_{cal} = M_{inst} + \Delta mag + Z_{Vega} \tag{2.1}$$

[5] All Gaia data was downloaded from the ESA archive: `https://gea.esac.esa.int/archive/`

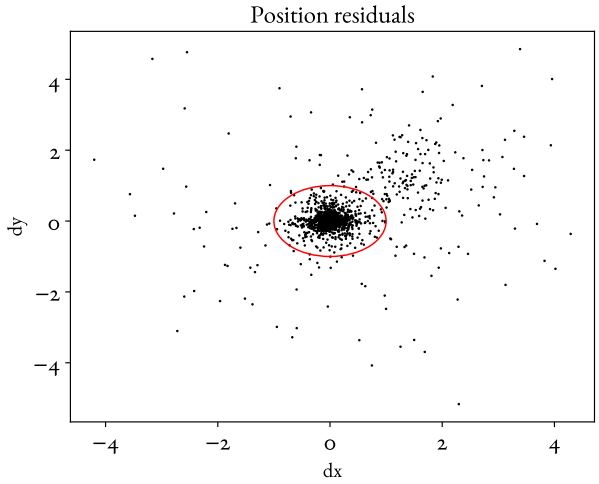

Figure 2.6: Removing Field Stars. A plot of the displacements in position for x and y, retrieved from the file in Step 1 of Section 2.6. The majority of points do not vary much amongst each other, and cluster around zero. Any points far away from this blob have a great variation in their proper motion, and are most likely field stars. Using the average size of the displacement as a guide, shown here as the red circle, these field stars were removed from the dataset. This step was repeated after plotting the CMD (see Section 3.1) to remove any lingering field stars before continuing with the data analysis.

where M_{cal} is the calibrated magnitude and M_{inst} is the instrumental magnitude. Z_{Vega} is the zero-point tied to the detector, which will vary by instrument, camera, and filter. The zero-points for the images in F275W and F814W were both retrieved online from their instrument's respective zero-point database[6].

Δmag is the median difference in flux between the `_flt` files and the `_drc` files, which describes our second zero-point needed for calibration. The `_drc` images have all been corrected for 1 sec of exposure time, such that the magnitude in 1 count per pixel is equivalent to 1 count per second. Before calculating the median, I first needed to derive a catalog of the magnitudes for the `_drc` files. This was done with the `drz_phot` program, which calculates the flux of each source through aperture photometry. The program takes several arguments, many of which will be familiar to the reader: `HMIN` — set to 10, to exclude any sources too close together, `FMIN` & `PMAX` — set to 0.1 and 9999 respectively, to include all sources, and arguments pertaining to the size of the aperture and annulus. The aperture radius, which tells the program the size of each source, could not be too large and accidentally incorporate other sources, but could not be too small either, and underestimate the flux. It was set to 10, equivalent to 0.5″. The minimum and maximum of the annulus, which is used to infer the sky background, was set to 14 and 20, corresponding to 0.7″ and 1″, respectively. The program then sums the flux within the given aperture and subtracts the sky background as set by the annulus to determine the magnitude

[6]The zero-points for *ACS/WFC* were taken from `https://acszeropoints.stsci.edu/`, and the zero points for *WFC3/UVIS* were taken from `https://www.stsci.edu/hst/instrumentation/wfc3/data-analysis/photometric-calibration/uvis-photometric-calibration`

for each source. It then returns a `.xym` file, containing the positions and magnitudes. To align this file with the data in each filter, the newly generated `.xym` files are passed through `xym1mat` with the final `MATCHUP` files for F275W and F814W. The resulting linker file will now have a magnitude that differs from the original data's magnitude by some constant — the zero-point, or Δmag. I then plotted this magnitude vs. the magnitude difference, and used the well-measured stars to calculate the median (Milone et al. 2023 [37]).

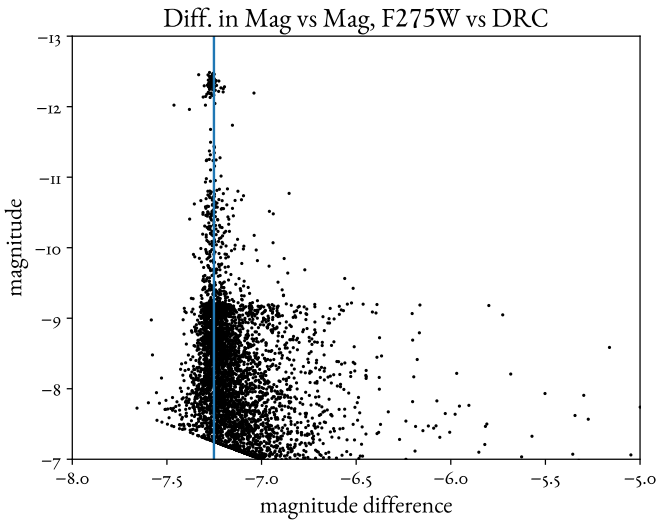

Figure 2.7: Calculating the Median. The plot of magnitude vs. difference in magnitude between F275W and the magnitude from the `_drc` file. Bright, non-saturated stars were used to calculate the median difference in magnitude for each file, shown here as a blue line. For F275W, the median difference was found to be 7.25, and 6.45 for F814W.

Once Δmag and Z_{Vega} were found, the magnitudes in each filter from the final linker file (the end result of Section 2.6) were calibrated following Equation 2.1. Following this reduction, I had now obtained the final photometric catalog that was utilized for the rest of this thesis, containing every well-measured stellar source, with positions expressed in the Gaia reference frame, and stellar magnitudes in F275W and F814W filters, expressed in the Vega photometric system.

3
Data Analysis

3.1 The CMD

After obtaining the full catalog, I then constructed the CMD, as shown in Figure 3.1. On the x-axis, for a representation of color/temperature, the magnitudes in each filter were subtracted from one another, and for the y-axis, for a representation of magnitude, the magnitude in the F814W filter was used. I repeated the process from Section 2.6 to plot the displacements in proper motion and remove any field stars before the rest of the analysis was done (see Figure 2.6). The standard components of a CMD[1] can be clearly seen, illustrating the different populations in the cluster. As expected, there is a sizable population of blue stragglers, shown to the left and the top of the MSTO.

3.2 Isochrone fitting

Once I had the CMD, I then wanted to fit the appropriate stellar isochrone to it. Stellar isochrones are curves which describe a set of stars of various masses, but the same age. They are representative of an SSP for a cluster and a useful way to determine the age of the population, as the position of the MSTO will move to the right as the age increases. This positioning is also affected by the metallicity, represented by the iron abundance [Fe/H], and the alpha abundance [α/Fe] (Salaris & Cassisi 2013 [13]). To represent an actual cluster, the calculation of a stellar isochrone must also take into account the effects of distance and interstellar extinction.

[1] As described previously, see the CMD displayed in Figure 1.2.

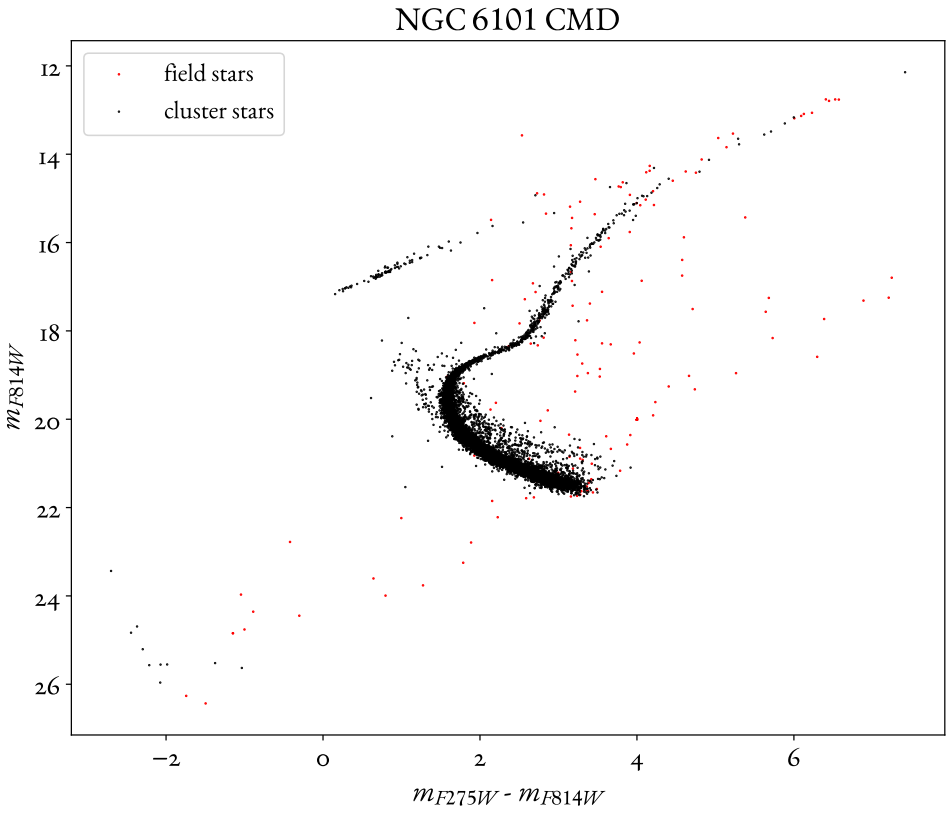

Figure 3.1: The CMD. The full CMD created for NGC 6101, after the data had been properly reduced. On the x-axis, the magnitudes of F275W and F814W were subtracted, giving a representation for color. On the y-axis is the magnitude for F814W, giving a representation for the luminosity. The field stars, which were then removed from the dataset, were marked in red.

Interstellar extinction, or reddening, occurs when the the light from a source passes through interstellar dust and clouds before reaching the observer. This material scatters the radiation, causing it to appear redder than it actually is. This effect is wavelength dependent, affecting shorter (bluer) wavelengths more than longer (redder) ones. It then follows that on a CMD, this extinction will cause the magnitude to shift to the right. To determine the difference in extinction between two different photometric bands, one can calculate the color excess, $E_\lambda(\lambda_1 - \lambda_2)$. The color excess between the Johnson U and V bands specifically, referred to as reddening, is often used to determine the interstellar extinction for any given photometric band. It can be calculated by:

$$A_\lambda = k_\lambda E(B - V) \tag{3.1}$$

Where A_λ is the absorption for a particular band observed at a wavelength λ, $E(B - V)$ is the reddening,

and k_λ is a constant corresponding with the particular filter used. Interstellar reddening is also affected by the position of the source, as the distribution of dust throughout the galaxy is not uniform. However, values of $E(B-V)$ for a source can be estimated using the Schlegel reddening map (see Schlegel et al. 1998 [41]), a composite $100\mu m$ map of extinction for the whole sky, found by calculating the dust temperature, which corresponds to a representation of dust column density.

Taking these parameters into account, theoretical isochrones can be derived by following models for stellar evolution and then corrected for extinction and distance. To fit NGC 6101 to an isochrone, I utilized the Dartmouth Stellar Evolution database[2] which provides isochrones with different ages and metallicities (see Dotter et al. 2008 [42]). As a starting point, I took values for the age, [Fe/H], [α/Fe], and distance from the literature. I then fit the cluster to an isochrone from the database, trying various combinations of these parameters within 1σ and adjusting this database isochrone for distance and interstellar reddening. Specifically, to find the best-fit isochrone, the corrected isochrone magnitudes are found with

$$I_{corr} = I_{mag} + \mu + A_\lambda \tag{3.2}$$

Where I_{mag} is the isochrone magnitude from the database, μ is the distance modulus, $\mu = 5\log(d) - 5$, where d is the distance in pc. A_λ is the interstellar extinction for a given photometric band, as previously discussed. $E(B-V) = 0.1040$, taken from an online database for the Schlegel reddening map[3], for the coordinates corresponding to the cluster. The values of k_λ for F814W and F275W were found to be 1.84 and 6.38 respectively, taken from HST's online records. The distance was set as $d = 14.50$ kpc, taken from Baumgardt & Vasiliev 2021 [43]. It derived an accurate distance using parallax from Gaia DR3, previous literature values, and HST observations.

The starting values for the isochrone parameters, as well as the ones found to best fit the cluster, can be seen in Table 3.1. The best-fit isochrone and its given parameters can be seen in Figure 3.2. As one can see, the isochrone is not a "perfect" fit — there is some slight deviation at the MSTO and the beginning of the RGB. It was, however, the best fitting isochrone found, utilizing values close to those reported in the literature.

Parameter	Literature	This Work
Age (Gyr)	13.0 ± 1	13.5
[Fe/H]	-1.98 ± 0.07	-1.95
[α/Fe]	0.2	0.2

Table 3.1: Isochrone parameters. The starting and best fit parameters for the stellar isochrone. The metallicity [Fe/H], originally obtained in Carretta et al 2009 [26], was derived using high-resolution spectroscopy. The values for [α/Fe] and age came from Dotter et al. 2010 [44], following the assumption that GCs with [Fe/H] < -1 have [α/Fe] = $+0.2$. Different combinations of the literature values were tried, following a step size of 0.01 for [Fe/H] and the age. The isochrone values which best fit the CMD, shown on the right, were all found to be within the bounds of the literature.

[2] https://rcweb.dartmouth.edu/stellar/

[3] https://irsa.ipac.caltech.edu/applications/DUST/

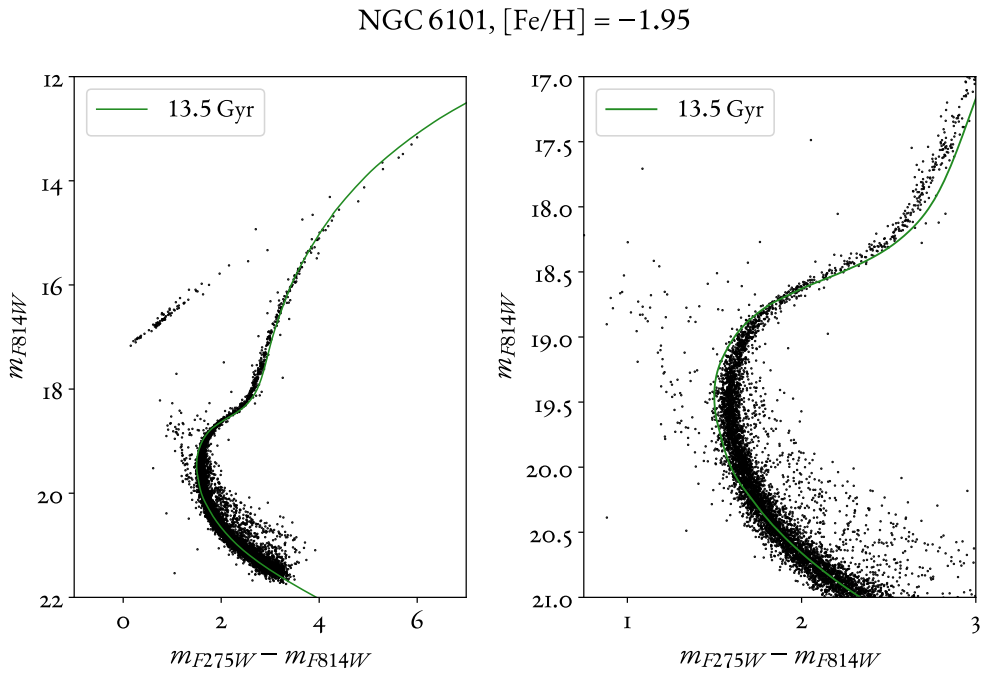

Figure 3.2: The best-fit isochrone. The best-fit isochrone, shown in green, determined for NGC 6101, corresponding to [Fe/H] = −1.95 and [α/Fe] = +0.2, giving an age of 13.5 Gyr.

3.3 The Luminosity Function

In order to obtain a mass function, I first needed to construct the luminosity function (LF) — simply, the number of stars per a determined magnitude interval. Before starting, I removed any data points equating to the AGB, HB, and WD populations. These stars have moved off the main sequence and follow their own trends in luminosity and mass; as such they are not relevant to characterizing the relationship between blue stragglers and binaries on the main-sequence. To derive the LF, I binned (see Figure 3.4) the clipped CMD into 11 bins. The bins above the MSTO had a length of 1 mag, and the bins below had a length of 0.4 mag. As shown in Figure 3.3, I then plotted the magnitude (in F814W) vs the log of the number of stars N found per bin. N was also divided by the length in bin, Δm, so all of the bins could be properly compared to each other.

Before plotting, each bin was corrected for completeness. Any given CMD will not have been able to pick up every star which occurs in a given bin, particularly at dimmer magnitudes, where the sources were measured with less precision and where the bulk of stars are found. The completeness correction numbers for each LF bin were provided by Professor Milone [45] and the bins were adjusted accordingly. As expected, these did not change the size of the bins significantly, with the exception of the dimmest bin, which was found to only be $\sim$ 25% complete. These completeness numbers for each bin were employed for the rest of the project, ensuring uniformity and accuracy for the analysis.

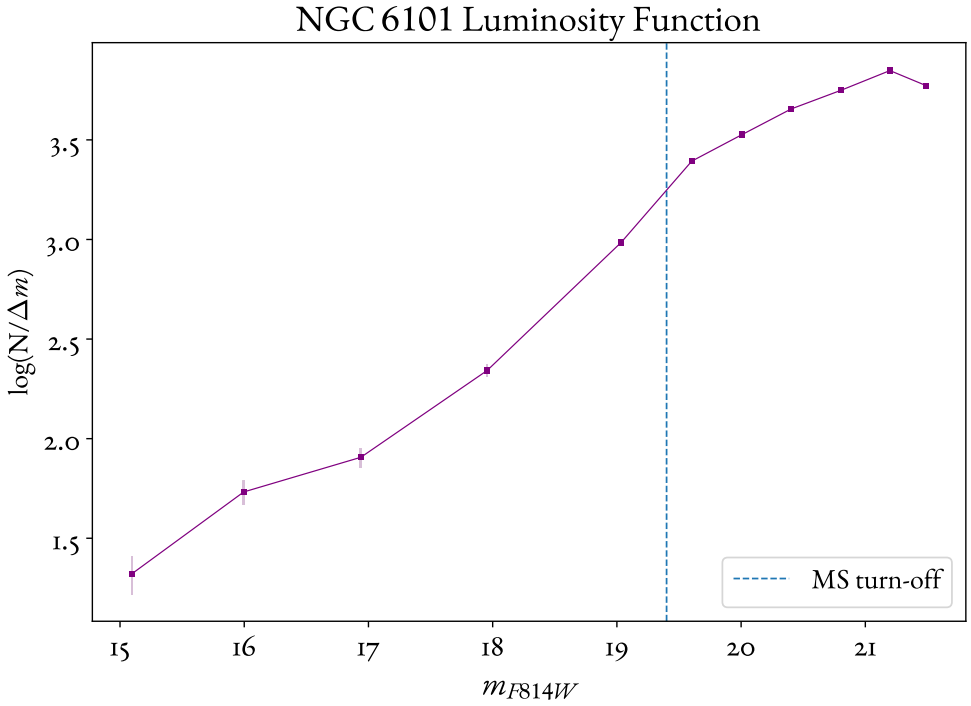

Figure 3.3: The luminosity function. The luminosity function constructed for NGC 6101, plotting the magnitude in F814W vs the logged number of stars per a given bin, N, divided by the length in bin, Δm. Bins before the MSTO, shown as a dotted blue line, corresponded to a difference of 0.4 mag, while bins above the MSTO had a length of 1 mag.

3.3.1 Error Calculation

The error in the number of stars per bin N is simply Poissonian counting error, $\sqrt{N}$. However, as the LF is represented through taking the log of the y-axis, it was essential it was propagated correctly, in order to account for the asymmetry of the upper and lower bounds. The error of the upper bound was calculated using

$$\sigma_{upper} = \log\left(\frac{N+\sqrt{N}}{\Delta m}\right) - \log\left(\frac{N}{\Delta m}\right) \tag{3.3}$$

It then follows that the lower bound for the error was calculated as

$$\sigma_{lower} = \log\left(\frac{N}{\Delta m}\right) - \log\left(\frac{N-\sqrt{N}}{\Delta m}\right) \tag{3.4}$$

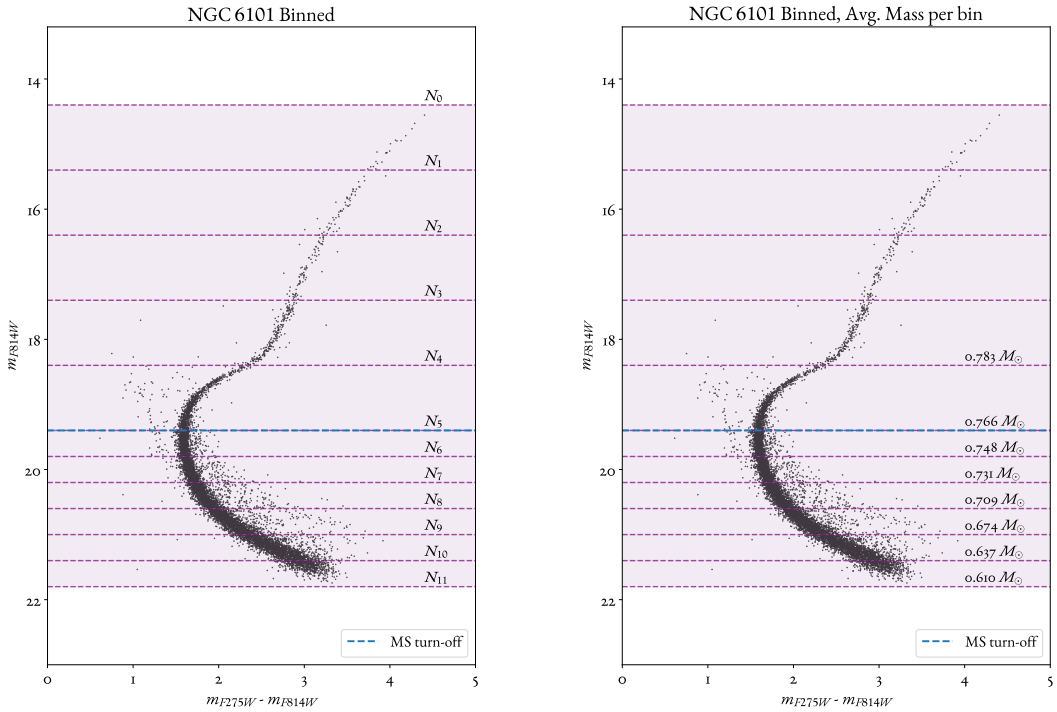

Figure 3.4: LF bins and corresponding mass. On the left, the chosen bins for the luminosity function of NGC 6101. 11 bins were chosen, with a size of $\Delta m = 1$ above the MSTO (the blue dotted line), and $\Delta m = 0.4$ below. On the right, the bins can be seen with their equivalent average mass in $M_\odot$, determined after the mass function was derived. Note that the highest mass equivalence ($0.783 M_\odot$) represented the average mass according to the top 4 bins averaged together, as the bins above the MSTO were simplified for the MF construction.

3.4 The Mass Function

Finally armed with the luminosity function, it was now possible to construct the mass function for the cluster. To convert the LF into an MF, I employed the mass-luminosity relation associated with the best-fit isochrone. As well as magnitude, the Dartmouth Database also supplies the initial mass, $M/M_\odot$, corresponding to the isochrone chosen. These mass values, from the isochrone fit in Section 3.2, were then interpolated for the magnitudes measured for the cluster, following a cubic spline procedure. Knowing which masses corresponded to which magnitudes, I could then construct the mass function, shown in Figure 3.5, by counting the number of stars N per mass interval ΔM. For the MF, both the x and y axes were logged. The y-axis was constructed in the same manner as the LF, as well as its error, following Section 3.3.1.

3.4.1 Bins above the turn-off

It is important to note that the relation given by the isochrone provides an initial mass — that is, the mass a star had as they entered the main-sequence. Subsequently, mass bins correlating to stars in the SGB and RGB cannot be trusted and were not used for analysis. Any representation of mass bins for the whole population of the cluster and the binary fraction above the MSTO are for illustrative purposes only; they were not considered for any calculations for the rest of this thesis. Excluding these bins, the MF is approximately flat, as is more clear in later representations of the MF(s) that will be illustrated in the succeeding Sections.

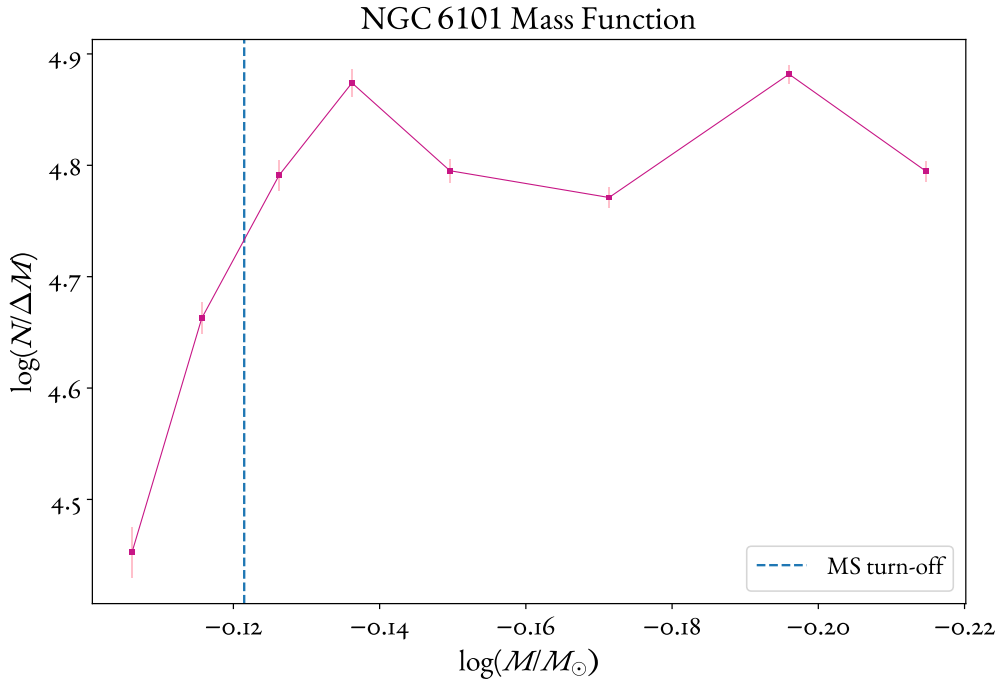

Figure 3.5: The mass function. The mass function constructed for all of NGC 6101, plotting the logged mass $M/M_{\odot}$ vs the logged number of stars per a given bin, N, divided by the length in bin, ΔM. As discussed in Section 3.4.1, the bins shown above the MSTO are for illustrative purposes only.

3.4.2 The Binary Mass Function

Once the total MF was derived, I moved on to constructing the MF for the binary population of the cluster. For an estimate of the binary population in NGC 6101, I used the total binary fraction f_{bin}^{TOT} determined by Milone et al 2012 [5] to be $f_{bin}^{TOT} = 0.096$. Assuming an approximately equal distribution of binaries throughout the cluster, composing the Binary MF is a straightforward process. I multiplied the N for each bin of the MF found previously by the given binary fraction, yielding the binary MF, shown

in Figure 3.6. As anticipated, the binary MF is the same shape as the total MF, and is approximately linear. In addition, I also constructed the binary MF averaged together in one bin[4] for an estimate of the total number of binaries in the cluster.

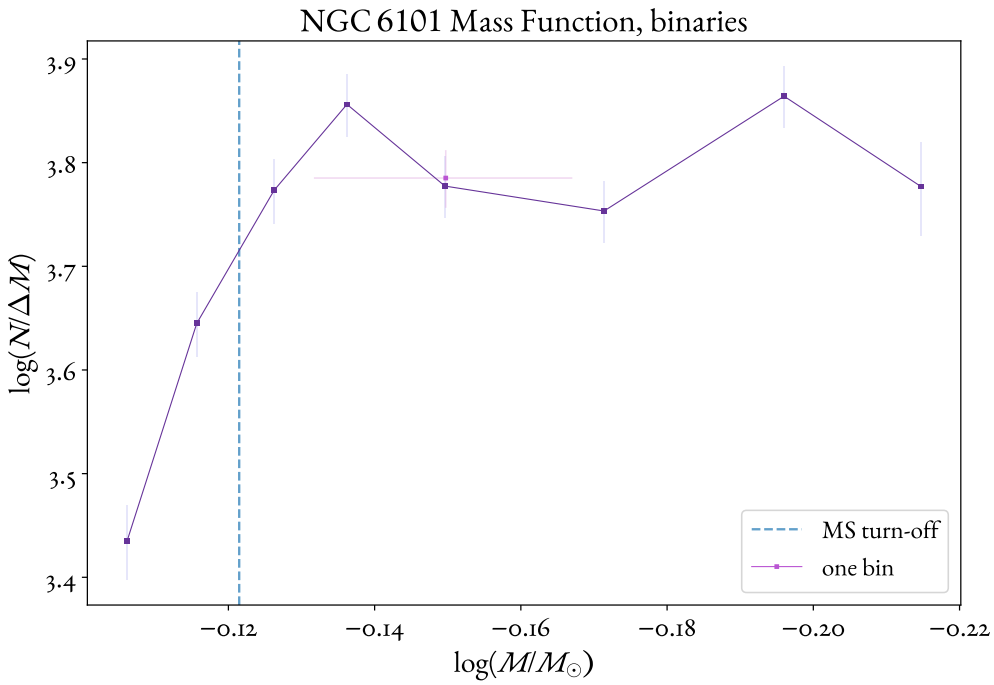

Figure 3.6: The binary mass function. The mass function constructed for the binary population of NGC 6101, plotting the logged mass $M/M_{\odot}$ vs the logged number of stars per a given bin, N, divided by the length in bin, ΔM. By definition it follows the same pattern as the total MF and can be approximated as flat.

3.5 BSSs Selection & Analysis

3.5.1 Selection

Before the luminosity and mass functions for BSSs can be derived, the blue straggler population must be determined through the CMD. Using the same algorithm as in Section 2.4.1, they were selected through visual inspection of stars which fit the traditional definition of a blue straggler. To exclude any unresolved main-sequence binaries that had evolved off the main-sequence, the isochrone estimation

[4]Only the first four bins before the MSTO were used to construct the "one bin" MF. The bins after the MSTO were disregarded (see Section 3.4.1) as well as the final bin, as it was more affected by photometric errors.

for equal-mass binaries was overlayed. The isochrone for this population was found using the best-fit isochrone for the cluster and shifting it right by 0.75 mag, corresponding to the position of such systems on the CMD, as was illustrated in Section 1.2. This process and the selected BSSs can be seen in Figure 3.7.

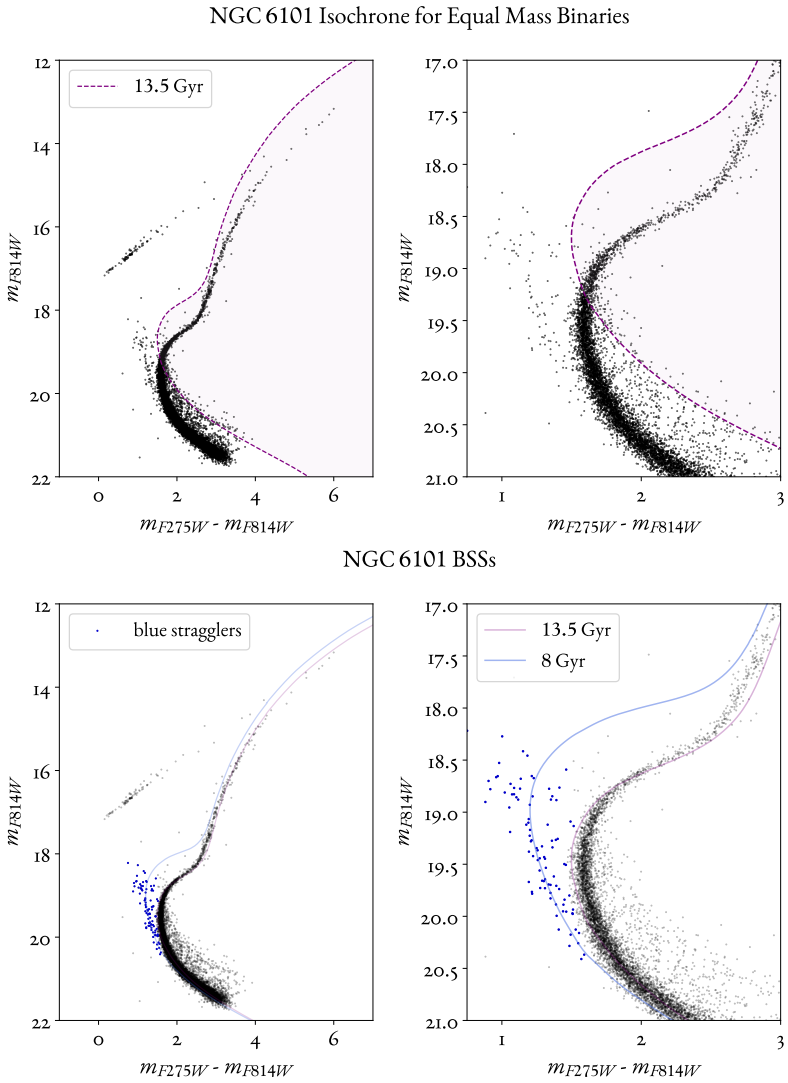

Figure 3.7: The BSS selection process. On the bottom, the blue stragglers population, seen in blue, for NGC 6101, after selection. Any stars that are not blue stragglers, but evolved MS-MS binaries were excluded by plotting their isochrone, seen on the top.

3.5.2 The BSS Luminosity Function

The LF for the blue straggler population was then constructed, following the same procedure as Section 3.3. The BSSs bins and LF are shown in Figure 3.8.

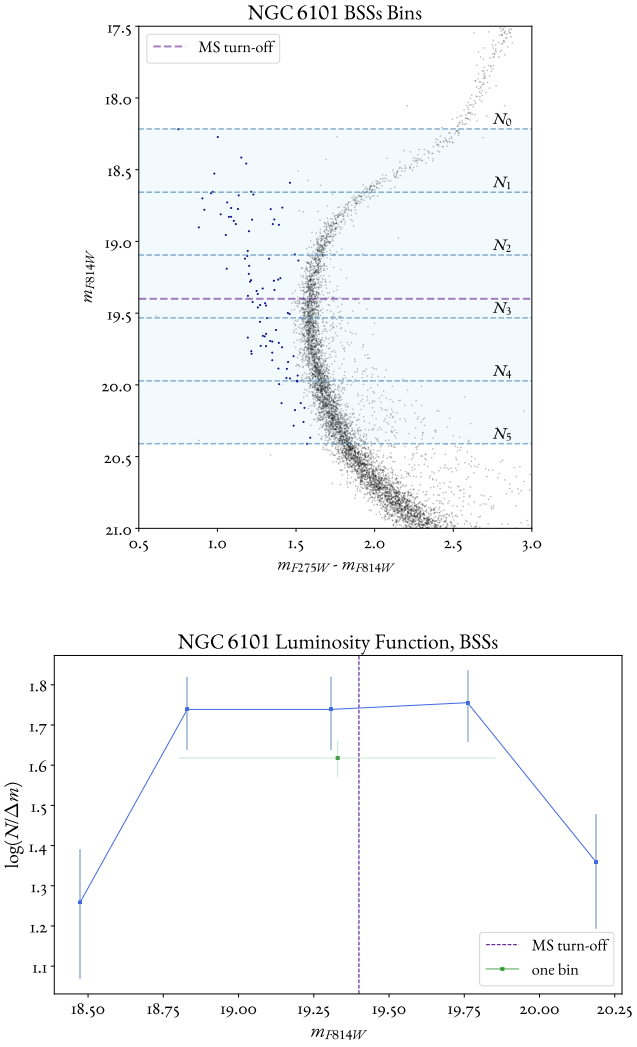

Figure 3.8: The BSS luminosity function. The luminosity function of the blue straggler population of NGC 6101, plotting the magnitude in F814W vs the logged number of stars per a given bin, N, divided by the length in bin, Δm. There were 5 bins chosen, which can be seen in the top figure.

3.5.3 The BSS Mass Function

To derive the mass-luminosity relationship needed to infer mass of BSSs, and thus develop the MF, I interpolated from the relation given from the isochrone which best-fit the population, as was done for the previous mass functions. However, there are few stipulations that follow when employing this method for blue stragglers. These isochrones were developed using traditional theories of stellar evolution, which by definition will not fit a given BSS population. Therefore, isochrones with the same parameters used for the host cluster, but much younger ages, are used to fit the population. But of course, we know these stars are not actually younger, and these isochrones do not account for the necessary adjustments needed in the stellar evolution. Masses inferred this way can then differ from the true BSS mass and should only be thought of as a rough approximation (Sills et al. 1997 [46]; Sills 2016 [12]). For NGC 6101 specifically, the BSS population is spread-out at higher magnitudes, making it difficult to chose a single isochrone that can appropriately characterize the entire population. The best-fit isochrone, shown in Figure 3.9, was found to be 8 Gyr, but the isochrones for 6 and 10 also fit the data fairly well. These uncertainties in mass measurement must be taken into consideration.

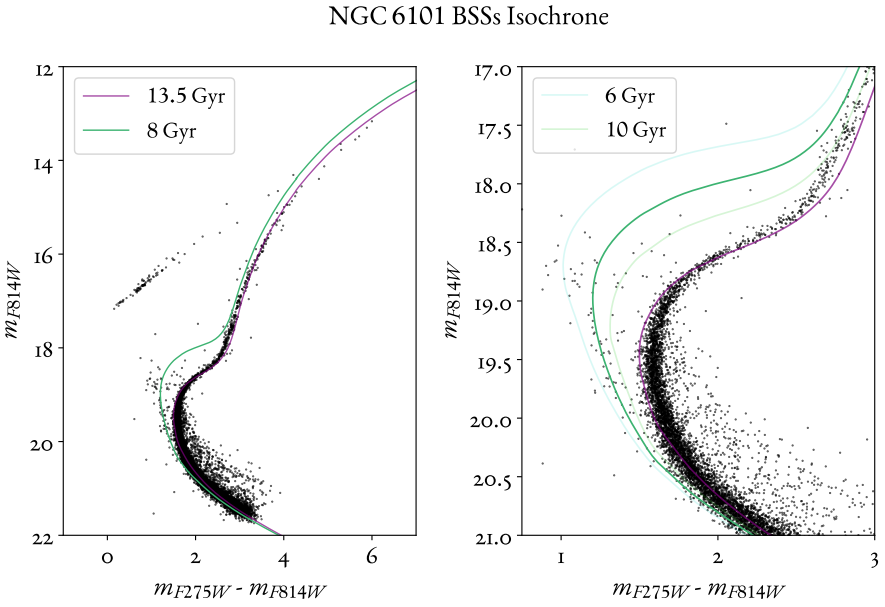

Figure 3.9: BSS isochrone fitting. The best-fit isochrone for the blue straggler population was found to be 8 Gyr, shown in green. It is important to note that fitting to an isochrone of 8 Gyr does not infer that the BSSs are 8 Gyr old, but rather have a mass corresponding to a normal star with an age of 8 Gyr. As there is a spread in the population, especially at greater magnitudes, there is some uncertainty in which isochrone is the best-fit. The isochrones for 6 and 10 Gyr, also shown on the right, could have also been chosen.

The MF was then created, utilizing the same process for the previous MFs. In addition, I also constructed the BSS MF averaged together in one point for an estimate of the total number of blue stragglers, as was done for the binary MF. It can be seen in Figure 3.10.

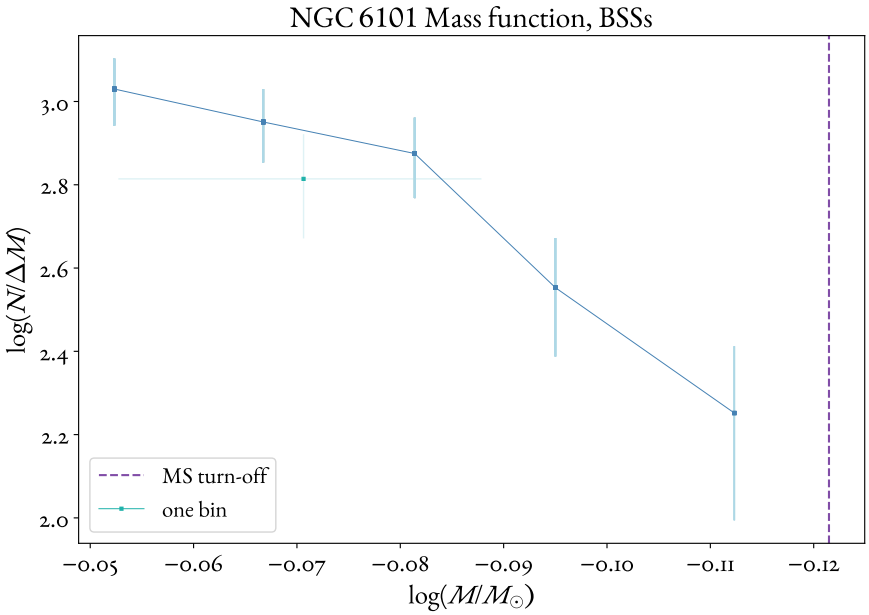

Figure 3.10: The BSS mass function. The mass function created for the blue straggler population in NGC 6101, plotting the logged mass $M/M_{\odot}$ vs the logged number of stars per a given bin, N, divided by the length in bin, ΔM. All of the bins were also averaged together in one bin, shown in green, for an estimate of the number of BSSs.

3.6 NGC 6101, as seen through MFs

It is now useful to visualize all of the mass functions developed for the cluster in Figure 3.11. It can be seen that both the total and binary MFs are approximately linear.

3.7 The BSS & Binary MF

Now that the mass functions for the binary fraction and the blue stragglers have been made, I could then try to relate them directly. After extrapolating the binary MF, I calculated the relationship between the two populations in a few different methods.

3.7.1 Binary Extrapolation

To relate the binary fraction, I wanted to get an estimate of the binary MF at the range of BSS MF to do a bin by bin comparison. To accomplish this, I linearly extrapolated the binary MF out to the magnitude (=mass) range of the blue stragglers, as seen in Figure 3.12.

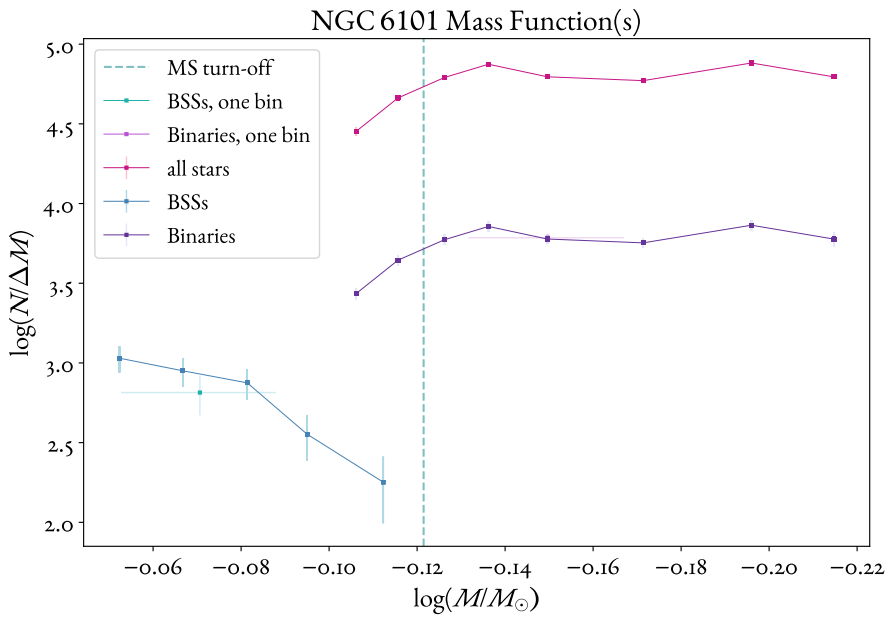

Figure 3.11: The MF(s) for NGC 6101. All of the mass functions for NGC 6101 created, overlayed in a single plot. As usual, it plots the logged mass $M/M_\odot$ vs the logged number of stars per a given bin, N, divided by the length in bin, ΔM.

3.7.2 Bin by bin comparison(s)

To quantify the relationship between binaries and blue stragglers, I tried three different comparisons, the results of which are summarized in Table 3.2:

- *Method 1 — Direct bin-by-bin comparison.*
  This method calculated the fraction of BSSs to binaries found for each bin. The last three[5] BSS bins — with average masses of $0.83M_\odot$, $0.80M_\odot$, and $0.77M_\odot$ — were directly compared to the equivalent bin from the extrapolated binary MF.
- *Method 2 — Average overall comparison.*
  This method calculated the fraction of BSSs to binaries through an estimation of the number of each population, found from the MFs averaged together in one bin.
- *Method 3 — Average comparison, with best-fit BSSs.*
  This method also calculated the fraction of BSSs to binaries from one average bin, except the BSS bin only considered those stars which were best described by the chose isochrone in Section 3.5.3. This corresponded to the blue stragglers found between 19.0 and 19.7 mag.

[5]The two first BSSs bins were less accurately measured, as the bins furthest away from the turn-off. As previously discussed, they were also not fit as accurately with the BSS best-fit isochrone.

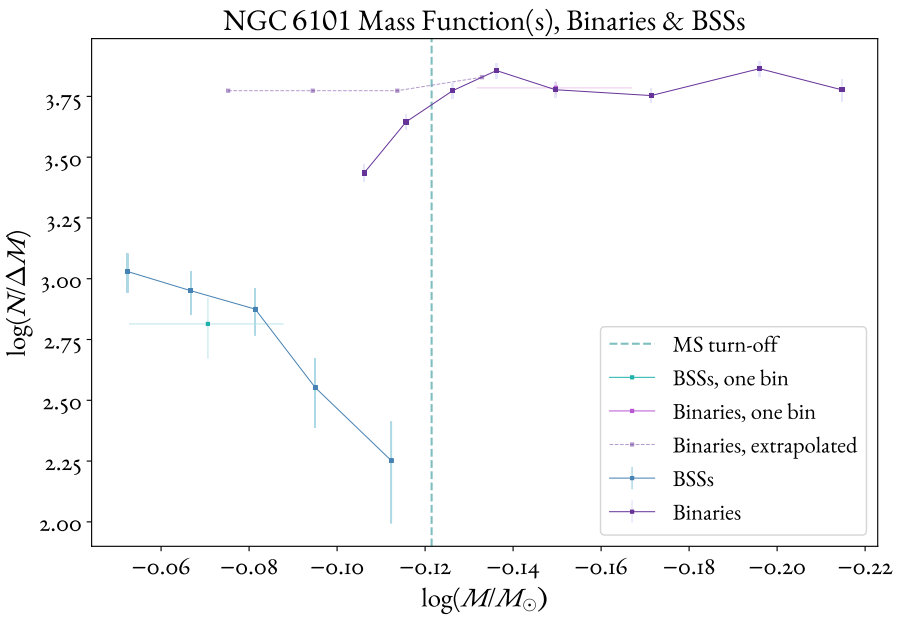

Figure 3.12: The BSS and Binary MFs. The mass functions derived for the binary and blue straggler population for NGC 6101. The binary mass function has been linearly extrapolated out to the range of the blue straggler mass function in order to compare the two.

Method 1	$12\% \pm 2$	$5\% \pm 3$	$4\% \pm 2$
Method 2		$10\% \pm 2$	
Method 3		$13\% \pm 2$	

Table 3.2: Results. The percentage of BSSs as compared to the binary fraction, found for each method.

All methods give a relationship around one order of magnitude of $\sim 10\%$. In this way, it can be estimated that about ten percent of binary systems in NGC 6101 may have evolved into BSSs.

4 Discussion

4.1 The BSS - Binary connection, revisited

Following the end of the previous Chapter, this thesis determined a measurable relationship between the blue straggler and binary population of NGC 6101. Utilizing initial mass functions constructed for each population, the estimated percentage of binary systems which may have evolved into BSSs was found to be roughly ten percent, consistent for the three different ways this relationship was derived. The idea of using mass functions to look at this relationship had not previously been explored in literature, hence it is difficult to compare this result directly to past studies. Regardless, this result does support previous ideas held about these populations. Binary systems are a major source for the formation of BSSs — possibly the dominant cause — so it would follow that there is a non-trivial numerical relationship between them. At the very least, this does support the previous correlations observed between binary and BSS frequency. On the other hand, while 10% is not an inconsequential number, it is not particularly high either. If binary systems are responsible for the vast majority of blue stragglers, should we expect a significant amount of the given binary fraction to evolve into them? Perhaps this project brought a result similar to that found by Leigh et al. 2013 [24], in which a connection between binaries and BSS certainly exists, but is not as strong as their other associations.

4.1.1 Uncertainties

There were various sources of uncertainty to this project, all of which could have affected the results. The masses inferred here all hinge on the mass-luminosity relation given from the best-fit isochrone, but none of the isochrones used were a precise fit of the data. This was particularly true for the BSS isochrone, especially as the population was spread at higher magnitudes (see Figure 3.9). For future

studies, a more statistics-based approach for isochrone determination should be taken. One example of this could be finding the best-fit isochrone through a median compiled from several different databases.

4.2 Moving forward

This project only looked at the relationship between binaries and blue straggler populations for a single cluster. To produce a statistically significant result, the approach outlined here should be repeated for a large dataset of clusters. In expanding this idea for a diverse group of GCs, it would also be interesting to notice if this result varies by other notable parameters, such as metallicity or mass segregation. As well, it would be advantageous for the process and its results to be replicated with simulations. This would ensure the approach has been rigorously tested, and confirm that the ensuing results are indeed robust and meaningful.

References

[1] R. Gratton, A. Bragaglia, E. Carretta, V. D'Orazi, S. Lucatello, and A. Sollima, "What is a globular cluster? An observational perspective,", vol. 27, no. 1, 8, p. 8, Nov. 2019.

[2] A. Renzini and A. Buzzoni, "Global properties of stellar populations and the spectral evolution of galaxies.," in *Spectral Evolution of Galaxies*, C. Chiosi and A. Renzini, Eds., ser. Astrophysics and Space Science Library, vol. 122, Jan. 1986, pp. 195–231.

[3] L. Greggio and A. Renzini, *Stellar Populations: A User Guide from Low to High Redshift*. Wiley-VCH, 2011.

[4] A. Renzini, "Finding forming globular clusters at high redshifts,", vol. 469, no. 1, pp. L63–L67, Jul. 2017.

[5] A. P. Milone *et al.*, "The ACS survey of Galactic globular clusters. XII. Photometric binaries along the main sequence,", vol. 540, A16, Apr. 2012.

[6] A. P. Milone *et al.*, "The binary populations of eight globular clusters in the outer halo of the Milky Way,", vol. 455, no. 3, pp. 3009–3019, Jan. 2016.

[7] D. Heggie and P. Hut, *The Gravitational Million-Body Problem: A Multidisciplinary Approach to Star Cluster Dynamics*. Cambridge University Press, 2003.

[8] A. Sollima, G. Beccari, F. R. Ferraro, F. Fusi Pecci, and A. Sarajedini, "The fraction of binary systems in the core of 13 low-density Galactic globular clusters,", vol. 380, no. 2, pp. 781–791, Sep. 2007.

[9] J. Ji and J. N. Bregman, "Binary Frequencies in a Sample of Globular Clusters. II. Sample Analysis and Comparison to Models,", vol. 807, no. 1, 32, p. 32, Jul. 2015.

[10] G. Piotto *et al.*, "Relative Frequencies of Blue Stragglers in Galactic Globular Clusters: Constraints for the Formation Mechanisms,", vol. 604, no. 2, pp. L109–L112, Apr. 2004.

[11] A. R. Sandage, "The color-magnitude diagram for the globular cluster M 3.,", vol. 58, pp. 61–75, Jan. 1953.

[12] A. Sills, "Blue stragglers: an observational overview.,", vol. 87, p. 475, Jan. 2016.

[13] M. Salaris and S. Cassisi, *Old stellar populations: How to study the fossil record of galaxy formation*. Wiley-VCH, 2013.

[14] F. R. Ferraro, N. D'Amico, A. Possenti, R. P. Mignani, and B. Paltrinieri, "Blue Stragglers, Young White Dwarfs, and UV-Excess Stars in the Core of 47 Tucanae,", vol. 561, no. 1, pp. 337–345, Nov. 2001.

[15] F. R. Ferraro *et al.*, "Dynamical age differences among coeval star clusters as revealed by blue stragglers,", vol. 492, no. 7429, pp. 393–395, Dec. 2012.

[16] J. Binney and S. Tremaine, *Galactic Dynamics: Second Edition*. Princeton University Press, 2008.

[17] F. R. Ferraro, B. Lanzoni, E. Dalessandro, A. Mucciarelli, and L. Lovisi, "Blue Straggler Stars in Globular Clusters: A Powerful Tool to Probe the Internal Dynamical Evolution of Stellar Systems," in *Ecology of Blue Straggler Stars*, H. M. J. Boffin, G. Carraro, and G. Beccari, Eds., ser. Astrophysics and Space Science Library, vol. 413, Jan. 2015.

[18] F. R. Ferraro *et al.*, "Discovery of Carbon/Oxygen-depleted Blue Straggler Stars in 47 Tucanae: The Chemical Signature of a Mass Transfer Formation Process,", vol. 647, no. 1, pp. L53–L56, Aug. 2006.

[19] M. B. Davies, "Blue straggler stars: formation channels,", vol. 87, p. 479, Jan. 2016.

[20] J. Lombardi, F. Rasio, and S. Shapiro, "Collisions of main-sequence stars and the formation of blue stragglers in globular clusters," *Astrophysical Journal*, vol. 468, no. 2 PART I, pp. 797–818, 1996, ISSN: 0004-637X.

[21] M. Mapelli, S. Sigurdsson, F. R. Ferraro, M. Colpi, A. Possenti, and B. Lanzoni, "The radial distribution of blue straggler stars and the nature of their progenitors,", vol. 373, no. 1, pp. 361–368, Nov. 2006.

[22] F. R. Ferraro *et al.*, "Two distinct sequences of blue straggler stars in the globular cluster M 30,", vol. 462, no. 7276, pp. 1028–1031, Dec. 2009.

[23] C. Knigge, N. Leigh, and A. Sills, "A binary origin for 'blue stragglers' in globular clusters,", vol. 457, no. 7227, pp. 288–290, Jan. 2009.

[24] N. Leigh, C. Knigge, A. Sills, H. B. Perets, A. Sarajedini, and E. Glebbeek, "The origins of blue stragglers and binarity in globular clusters,", vol. 428, no. 1, pp. 897–905, Jan. 2013.

[25] G. Cozens, A. Walsh, and W. Orchiston, "James Dunlop's historical catalogue of southern nebulae and clusters," *Journal of Astronomical History and Heritage*, vol. 13, no. 1, pp. 59–73, Mar. 2010.

[26] E. Carretta, A. Bragaglia, R. Gratton, V. D'Orazi, and S. Lucatello, "Intrinsic iron spread and a new metallicity scale for globular clusters,", vol. 508, no. 2, pp. 695–706, Dec. 2009.

[27] R. E. Cohen, A. Sarajedini, K. Kinemuchi, and R. Leiton, "The Unusual RR Lyrae Population of NGC 6101,", vol. 727, no. 1, p. 9, Jan. 2011.

[28] G. A. Rutledge *et al.*, "Galactic Globular Cluster Metallicity Scale from the Ca II Triplet I. Catalog,", vol. 109, pp. 883–906, Aug. 1997.

[29] E. Dalessandro, F. R. Ferraro, D. Massari, B. Lanzoni, P. Miocchi, and G. Beccari, "No Evidence of Mass Segregation in the Low-mass Galactic Globular Cluster NGC 6101,", vol. 810, no. 1, p. 40, Sep. 2015.

[30] M. Peuten, A. Zocchi, M. Gieles, A. Gualandris, and V. Hénault-Brunet, "A stellar-mass black hole population in the globular cluster NGC 6101?", vol. 462, no. 3, pp. 2333–2342, Nov. 2016.

[31] Ryon, J. E. Stark, D. V, *Acs instrument handbook, version 23.0*, STScI, Baltimore, 2023.

[32] Marinelli, M. Dressel, L., *Wide field camera 3 instrument handbook, version 16.0*, STScI, Baltimore, 2024.

[33] J. Anderson and I. R. King, "Toward High-Precision Astrometry with WFPC2. I. Deriving an Accurate Point-Spread Function," *Publications of the Astronomical Society of the Pacific*, vol. 112, no. 776, pp. 1360–1382, Oct. 2000, ISSN: 1538-3873.

[34] J. Anderson and I. R. King, *PSFs, Photometry, and Astronomy for the ACS/WFC*, Instrument Science Report ACS 2006-01, 34 pages, Feb. 2006.

[35] J. Anderson *et al.*, "Deep Advanced Camera for Surveys Imaging in the Globular Cluster NGC 6397: Reduction Methods,", vol. 135, no. 6, pp. 2114–2128, Jun. 2008.

[36] S. T. Sohn, J. Anderson, and R. P. van der Marel, "The M31 Velocity Vector. I. Hubble Space Telescope Proper-motion Measurements,", vol. 753, no. 1, 7, p. 7, Jul. 2012.

[37] A. P. Milone *et al.*, "Hubble Space Telescope survey of Magellanic Cloud star clusters. Photometry and astrometry of 113 clusters and early results,", vol. 672, A161, Apr. 2023.

[38] Gaia Collaboration, "The Gaia mission,", vol. 595, A1, Nov. 2016.

[39] Gaia Collaboration, "Gaia Data Release 3. Summary of the content and survey properties,", vol. 674, A1, Jun. 2023.

[40] Stevens, Mark, *Hst data handbook, version 3.1*, STScI, Baltimore, 1998.

[41] D. J. Schlegel, D. P. Finkbeiner, and M. Davis, "Maps of Dust Infrared Emission for Use in Estimation of Reddening and Cosmic Microwave Background Radiation Foregrounds,", vol. 500, no. 2, pp. 525–553, Jun. 1998.

[42] A. Dotter, B. Chaboyer, D. Jevremović, V. Kostov, E. Baron, and J. W. Ferguson, "The Dartmouth Stellar Evolution Database,", vol. 178, no. 1, pp. 89–101, Sep. 2008.

[43] H. Baumgardt and E. Vasiliev, "Accurate distances to Galactic globular clusters through a combination of Gaia EDR3, HST, and literature data,", vol. 505, no. 4, pp. 5957–5977, Aug. 2021.

[44] A. Dotter *et al.*, "The ACS Survey of Galactic Globular Clusters. IX. Horizontal Branch Morphology and the Second Parameter Phenomenon,", vol. 708, no. 1, pp. 698–716, Jan. 2010.

[45] A. P. Milone, *Private communication*, 2024.

[46] A. Sills, J. Lombardi James C., C. D. Bailyn, P. Demarque, F. A. Rasio, and S. L. Shapiro, "Evolution of Stellar Collision Products in Globular Clusters. I. Head-on Collisions,", vol. 487, no. 1, pp. 290–303, Sep. 1997.

Acknowledgments

I would like to thank my supervisor, Professor Antonino Milone, for his invaluable assistance, direction, and support throughout this project. Additionally, I am very grateful for my family and their encouragement that they provided, even from afar. Particularly, I am most thankful for my mother, as without her insistence that I give studying abroad a try, I would not be here. Finally, this thesis would not have been possible without the friends that I had the utmost privilege of meeting during my time in Padova. I thank them immensely for their companionship over the last two and a half years, and for all of the adventures we traversed together, from climbing a Nikola Telsa statue in Belgrade, to morning cappuccinos before studying in Specola. Although $\sim$ 4000 kilometers stand before me and my family in Florida, they always made me feel right at home.